Materials Science & Engineering A 817 (2021) 141370

Contents lists available at ScienceDirect

Materials Science & Engineering A

journal homepage: www.elsevier.com/locate/msea

Deformation behavior and strengthening mechanisms in a CNT-reinforced bimodal-grained aluminum matrix nanocomposite

S.M.A.K. Mohammed [a], D.L. Chen [a,*], Z.Y. Liu [b], D.R. Ni [b], Q.Z. Wang [b], B.L. Xiao [b], Z.Y. Ma [b,**]

[a] Department of Mechanical and Industrial Engineering, Ryerson University, Toronto, Ontario, M5B 2K3, Canada
[b] Shi-changxu Innovation Center for Advanced Materials, Institute of Metal Research, Chinese Academy of Sciences, 72 Wenhua Road, Shenyang 110016, China

ARTICLE INFO

Keywords:
Metal matrix nanocomposites
Bimodal grain structure
Carbon nanotube
Deformation behavior
Strengthening mechanisms

ABSTRACT

The aim of this study was to identify deformation behavior and strengthening mechanisms of a carbon nanotube (CNT)-reinforced bimodal-grained Al–Cu–Mg nanocomposite and its base alloy fabricated by two-step ball milling, powder metallurgy and extrusion. A superior strength-ductility synergy stemming from the concurrent presence of ultrafine grains (UFGs) and coarse grains (CGs) was achieved. Singly-dispersed CNTs in UFGs and sound CNT/Al interfacial bond contributed to a significant improvement in the strength of the nanocomposite. The predominant strengthening mechanism in the CNT-reinforced nanocomposite was identified to be Orowan looping due to severe shearing of CNTs into nano-sized fragments during ball milling, along with load-transfer and thermal mismatch-induced dislocation strengthening mechanisms. The predicted yield strength of the nanocomposite was in agreement with the experimental value obtained. The findings in this study help pave the way for developing high-performance lightweight materials with a superior strength-ductility synergy via incorporating CNTs with novel bimodal grain structures.

1. Introduction

Ultrafine-grained metal matrix nanocomposites (MMNCs) containing nano-reinforcements exhibit high strengthening effects [1–3]. Carbon nanotube (CNT) is one of the most promising nano-reinforcement candidates in MMNCs owing to its high strength, elastic modulus and nanometer size along with its excellent electrical and thermal conductivities [4,5]. As such, CNT-reinforced aluminum matrix nanocomposites (AMNCs) have received a great deal of attention [6,7]. The strengthening in such nanocomposites is primarily attributed to load transfer, dislocation strengthening, and Orowan strengthening [7–9]. The main strengthening mechanism in CNT-reinforced nanocomposites in the case of high aspect ratio of CNTs is reported to be load transfer [10,11]. However, CNTs are normally shortened due to the shearing effect during high-energy ball milling (HEBM), thereby decreasing the length or aspect ratio of CNTs and increasing the potential significance of Orowan strengthening based on their interaction with dislocations [12,13].

The ultrafine-grained MMNCs often exhibit high strength but low ductility stemming from the insufficient ductility in the matrix, which impedes their structural applications [14]. To solve the strength-ductility trade-off dilemma, tailoring/engineering the microstructure with a distribution of grain sizes via proper processing techniques was proposed as an effective strategy. For example, heterogeneous [15–17], gradient [18], or bimodal [19–21] grain distributions have been observed to demonstrate a synergetic increase in strength and ductility. One of the most effective methods of fabricating such a grain distribution is to introduce coarse grains (CGs) in the ultrafine-grains (UFGs) to achieve a balanced mechanical properties [17,22,23]. Under these circumstances geometrically necessary dislocations (GNDs) would be generated near the boundaries between the CGs and UFGs, and gradually enhance the strength of CGs to be close to that of UFGs. As a result, the deformation behavior of bimodal-grained materials is different from that of pure coarse-grained or ultrafine-grained materials. The addition of CNTs into such a bimodal-grained matrix is anticipated to further enhance the strength. Thus, the underlying strengthening mechanisms in such a CNT-reinforced bimodal-grained nanocomposite need to be explored.

The present study was undertaken with three primary objectives: Firstly, fabricate a unique CNT-reinforced bimodal-grained Al–Cu–Mg

* Corresponding author.
** Corresponding author.
E-mail addresses: dchen@ryerson.ca (D.L. Chen), zyma@imr.ac.cn (Z.Y. Ma).

https://doi.org/10.1016/j.msea.2021.141370
Received 4 February 2021; Received in revised form 18 April 2021; Accepted 20 April 2021
Available online 4 May 2021

nanocomposite and base alloy with high strength and ductility; secondly, characterize microstructure-strength relationship; and finally, identify and quantify the underlying strengthening mechanisms and validate with experimental results. Multiple strengthening mechanisms including load transfer, dislocation strengthening and Orowan looping are taken into consideration to elucidate the enhanced mechanical properties in CNT-reinforced Al–Cu–Mg nanocomposite.

2. Methods

2.1. Raw material and fabrication

Atomized 2009Al (Al-4wt.%Cu-1.5 wt%Mg) powders with a diameter of ~10 μm were used as raw materials. The CNTs of ~98% purity with an outer diameter of 10–30 nm, provided by Tsinghua University were prepared via chemical vapor deposition (CVD). The as-received 2009Al powders mixed with 4 vol% CNTs were milled in an attritor at 400 rpm for 6 h with a ball-to-powder mass ratio of 15:1. The ball-milled powders were further mixed with 25 vol% as-received 2009Al powders using a dual axis mixer at 50 rpm for 6 h, thereby obtaining nanocomposite powders with a unique bimodal-grained microstructure composed of UFG (75%, with 4 vol% CNT) and CG (25%). Thus, the final fraction of CNTs in the nanocomposite powders became 3 vol%.

The nanocomposite powders were cold compacted and vacuum hot pressed into billets under a pressure of 50 MPa at 560 °C, followed by extrusion at 430 °C at a high extrusion ratio (ER) of 16. Thus, the nanocomposite was fabricated by combination of HEBM, powder metallurgy (PM) and extrusion processing. The extruded bars were subsequently solution treated at 500 °C for 2 h, quenched into water and naturally aged. An 2009Al base alloy without CNTs was also prepared in a similar manner for reference. The bimodal-grained 2009Al alloy and CNT/2009Al nanocomposite will be referred to as B-AA and B-CNT/AA from here on, where B stands for "bimodal".

2.2. Property characterization

After grinding using emery papers from #400 to #4000 grits, and diamond-paste polishing down to 0.5 μm, the metallographic samples were etched with Keller's reagent for 60 s. EBSD samples were electropolished using an electrolyte containing 10 mL $HClO_4$ and 90 mL ethanol at 20 V for 30 s at a room temperature. A scanning electron microscopy (SEM, JSM-6380LV) and a transmission electron microscopy (TEM, Tecnai G2 20) were used to study the microstructural features. Phase analysis was carried out on PANalytical X-ray diffractometer with Cu K_α radiation ($\lambda = 0.154$ nm) at 45 kV and 40 mA with a diffraction angle from 20° to 90° at a scanning rate of 0.05° s^{-1}. Tensile specimen with a gauge length of 25 mm (see Fig.S1) were tested at strain rates of 1 $\times 10^{-6}$ s^{-1} and 1 $\times 10^{-4}$ s^{-1} using a universal United testing system at room temperature. At least two samples were tested at each strain rate.

3. Results

3.1. Microstructure

The microstructural features of the extruded B-AA and B-CNT/AA in T4 condition are shown in Figs. 1 and 2, respectively. The microstructures consisted of a mixture of UFG (equiaxed) matrix with ~25% CG (columnar) bands or lamellae that align in the extrusion direction (ED), see supplementary Fig.S2. The reduction in the grain size of both materials was in general attributed to ball milling, and dynamic recrystallization (DRX) that occurred during plastic deformation at higher working temperatures [5]. The average grain size in UFG zone was ~100–300 nm and no further refinement could be possible even with the addition of CNTs as the UFGs are below lower limit of sub-grain size (~2 μm) [5]. Significant differences of neighboring grains in the B-AA and B-CNT/AA could be seen from the EBSD orientation angles in Figs. 1(a) and **2(a)**, where the low-angle and high-angle grain boundaries (denoted as LAGBs and HAGBs) were defined by misorientation angles between adjacent grains of 2–15° and >15°, respectively. During ball milling the dislocations are rearranged, leading to the formation of HAGBs along with some LAGBs. The distinct CG and UFG regions in the B-AA and B-CNT/AA could be seen from the orientation maps in **Figs. 1 (b)** and **2(b)**. The majority of CGs are oriented along <111> which is also the extrusion direction due to the large extrusion ratio of 16, while UFGs are largely randomly oriented in both materials. The Kernel average misorientation (KAM) graphs that reflect the local lattice distortion and strain energy within the grains are shown in Figs. 1(c) and **2(c)** for the base alloy and nanocomposite, respectively. The base alloy appeared to show somewhat higher local lattice distortions, suggesting a higher dislocation density in the nanocomposite compared with its base

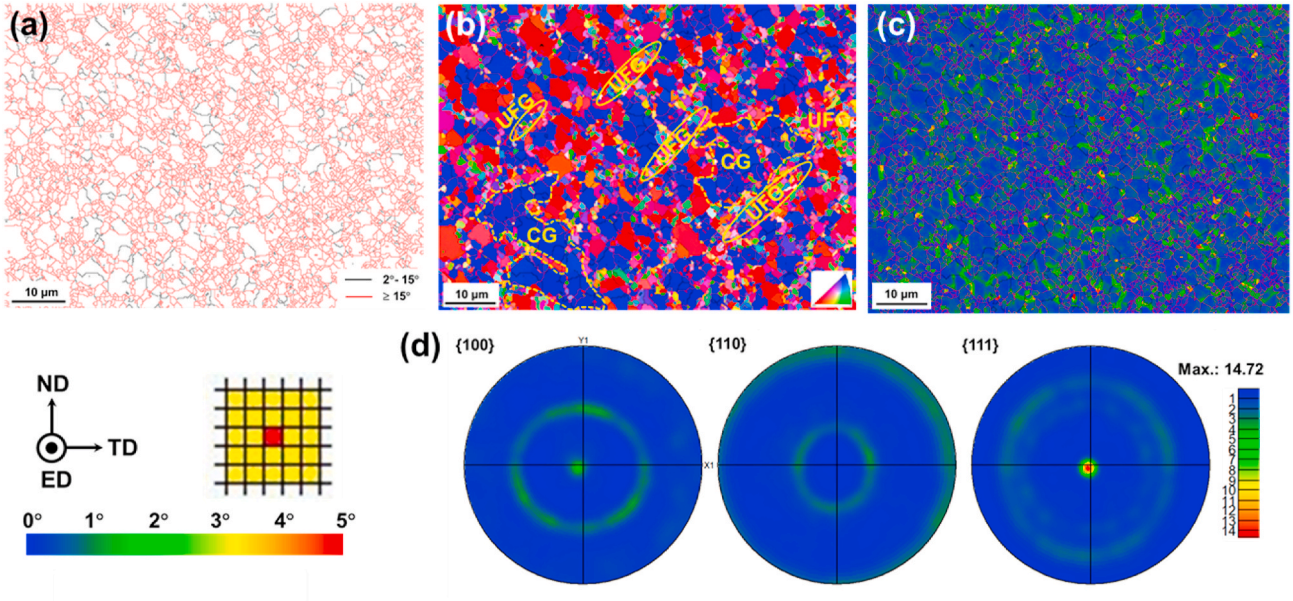

Fig. 1. EBSD results of bimodal-grained 2009Al alloy: **(a)** grain misorientation angle, **(b)** orientation map, **(c)** KAM map, and **(d)** pole figures perpendicular to the extrusion axis.

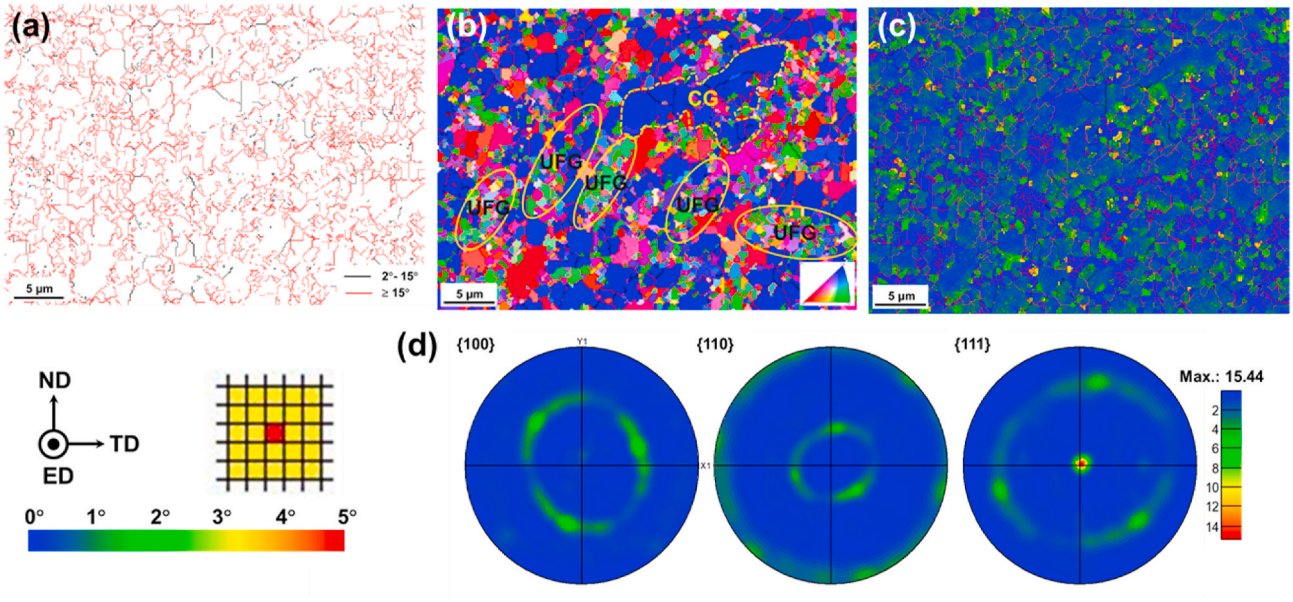

Fig. 2. EBSD results of bimodal-grained CNT/2009Al nanocomposite: **(a)** grain misorientation angle, **(b)** orientation map, **(c)** KAM map, and **(d)** pole figures perpendicular to the extrusion axis.

alloy which will be confirmed via XRD.

As revealed by orientation maps in Figs. 1(b) and **2(b)** and pole figures in Figs. 1(d) and **2(d)**, the orientation of grains, especially CGs, is more pronounced along the ED or along <111> direction, suggesting the presence of <111> fiber texture in the extruded Al matrix and B-CNT/AA, with a maximum intensity of ~14.7 and ~15.4 MRD (multiple of a random distribution), respectively. Such a <111> fiber texture is often observed in the extruded Al alloys [24]. This is due to severe plastic deformation (SPD) experienced by the samples mainly during hot extrusion. Besides, it would be reasonable to consider a fraction of deformed grains along with some sub-grained structures (see supplementary Fig.S3**)**. It should be noted that the indexing of EBSD mapping was ~75%, indicating that a portion of UFGs might be smaller than the spatial resolution limit in EBSD. The unidentified voids were eliminated using noise reduction during data analysis. To overcome this, TEM and high-resolution TEM (HRTEM) will be utilized to characterize the microstructure of the B-CNT/AA nanocomposite and provide more information in the later section.

3.2. X-ray diffraction

X-ray diffraction (XRD) investigations were carried out to identify the phases present in the B-AA and B-CNT/AA, as illustrated in **Fig. 3**. The diffusion of Cu into Al matrix led to the formation of observed Al_2Cu peaks in both materials. Meng et al. [25] conducted XRD analysis of a CNT/Al–Cu nanocomposite at different stages of fabrication and reported that sintering was more responsible for alloying than ball milling which also led to the formation of Al_2Cu. With the addition of CNTs in the alloy, a couple of small Al_4C_3 peaks were observed in the B-CNT/AA which confirms the reaction between Al and CNTs. The formation of Al_4C_3 to a certain extent is an indication of a strong bond between the reinforcement and matrix. The other characteristic observation evaluated from the XRD patterns is dislocation density (ρ), which could be estimated as [26],

$$\rho = \frac{\beta^2}{4.35\, b^2}, \quad (1)$$

where b is the Burgers vector of Al (=0.286 nm), β ($=\beta_{obs}-\beta_{inst}$) is the full width at half maximum (FWHM) of Al peaks, β_{obs} and β_{inst} are the observed and instrumental peak broadening, respectively. The

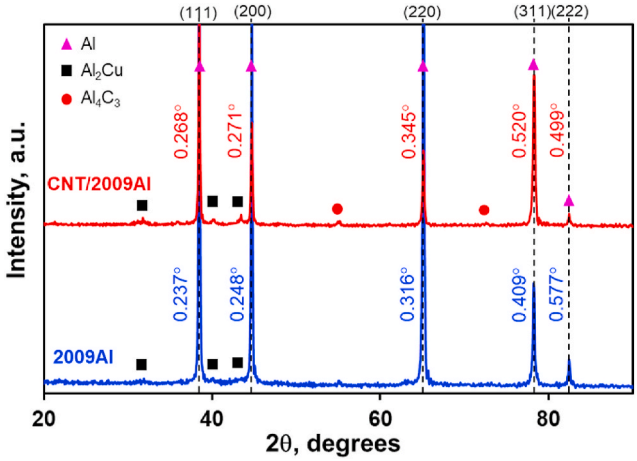

Fig. 3. X-ray diffraction patterns of bimodal-grained 2009Al alloy and CNT/2009Al nanocomposite after T4 heat-treatment, where the values given beside each peak are the full width at half maximum (FWHM).

instrumental peak broadening is corrected using pure Al powders. The dislocation density in this study is taken as an average value at five significant peaks (111), (200), (220), (311) and (222) detected from the XRD analysis (Fig. 2). The individual values at each peak for both materials are presented in supplementary Table S1. In general, the ρ value increased with the peak position for both materials. Then the average dislocation density of B-AA and B-CNT/AA was obtained to be 5.5×10^{13} m^{-2} and 6.4×10^{13} m^{-2}, respectively. A similar magnitude of dislocation densities was also obtained in CNT/Al nanocomposites by Xu et al. [27]. The high dislocation density was basically attributed to the strain accumulation in the samples due to SPD during ball milling [28]. However, the somewhat higher dislocation density in the B-CNT/AA was further related to the presence of CNTs, which was in agreement with the result from the KAM maps (Figs. 1(c) and 2(c)).

3.3. Tensile properties

The tensile properties evaluated from the engineering stress-strain

curves at strain rates of 1×10^{-6} s^{-1} and 1×10^{-4} s^{-1} are presented in Table 1. The results of unimodal 2009Al fabricated by PM are also presented for the sake of comparison although the grain size was different [29]. A significant increase in the yield strength (YS) by ~85% and ultimate tensile strength (UTS) by ~49% was observed in B-AA with equivalent ductility, compared with the unimodal microstructure. No significant strain-rate dependence of the properties was present. Further higher YS and UTS were achieved with the addition of 3 vol% CNTs in the B-AA but with lower ductility. The higher strength and loss of ductility are attributed to the higher dislocation density [27].

The Young's modulus evaluated from the tensile curves was 76.3 ± 2.7 and 90.7 ± 3.5 GPa for B-AA (E_m) and B-CNT/AA (E_C), respectively. The slightly higher value in B-AA than that of pure Al was because of alloying and HEBM. Increase in the Young's modulus with milling time was reported for Al alloys, which was related to homogeneous dispersion and better bonding between the powders during milling and secondary processing such as compaction and sintering [28]. The further increase in E_C by ~19% was related to the addition of CNTs and their random distribution in the matrix, to be revealed via TEM examinations and also reported in Ref. [30].

4. Discussion

Fig. 4 presents typical TEM images showing a remarkable bimodal grain distribution and CNT dispersion, and a HRTEM image showing the matrix-CNT interface structure in the nanocomposite. The microstructure observed via TEM in Fig. 4(a) consisting of distinctive CGs and UFGs in layers is consistent with that via EBSD (Fig. 2) and OM (Fig.S2). Second-phase Al_2Cu particles can be clearly seen from the TEM images as indicated by arrows. As well, CNTs were observed to be randomly dispersed in the Al matrix in a uniform manner (Fig. 4(b)). Due to the damage caused during HEBM, the length of CNTs (L_{CNT} = ~200 nm [23]) appeared to be much smaller than the as-received ones (Fig. 4(b)). The critical length of CNTs for effective load transfer strengthening could be estimated as $L_c = \sigma_{CNT} \times d/2\tau_o$, where σ_{CNT} is the tensile strength of CNTs (= ~30 GPa [31]), d is the diameter of CNTs (=10–30 nm), and τ_o is the shear stress of matrix (~$\sigma_{ym}/2$, with σ_{ym} being the YS of matrix). Then the estimated L_c is ~543–1628 nm, which is much larger than the actual length of CNTs in the present nanocomposite (Fig. 4(b)). It is thus anticipated that other mechanisms such as Orowan strengthening would play an important role, which will be discussed later. Fig. 4(c) shows that the tube structure of the CNTs was well retained, the CNT/Al interfaces were well bonded, and no voids were detected. The formation of Al_4C_3 has been discussed in the previous investigation [11]. Based on these observations, a schematic is plotted in Fig. 4(d) to illustrate the bimodal grain distribution of the material in layered fashion.

The tensile stress-strain curves of B-AA and B-CNT/AA at strain rates of 1×10^{-6} s^{-1} and 1×10^{-4} s^{-1} are presented in Fig. 5(a). The obvious increase in the strength with appreciable ductility is due to the concurrent presence of UFGs and CGs. The UFGs offer more grain boundaries which eventually lead to a superior strength based on the Hall-Petch relationship. The CGs are able to accommodate more dislocations with a higher dislocation storage capacity which results in a high ductility. A similar increase in strength and ductility of bimodal-grained Al–Mg alloys is reported in Refs. [21,32]. As seen in the inset of Fig. 5(a), the B-AA and B-CNT/AA samples fractured at an angle of ~45° and ~0° to the loading direction which exemplify relatively ductile and brittle nature of failure. As the base alloy failed in a ductile manner at an angle of ~45° which is a plane of the maximum shear stress, with the varying height of the fractured surface shown in Fig.S4.

Fig. 5(b) presents a schematic of deformation behavior of bimodal-grained alloy which can typically be distinguished into three stages. Stage I is conventional, where both CG and FG materials deform elastically. In stage II CGs deform plastically and FGs deform elastically, leading to deformation incompatibility. Although CGs can accommodate more strain due to the higher dislocation storage capacity, FGs adjacent to CGs attempt to coordinate as well until the onset of plastic deformation in FGs. This results in strain gradients substituted by the pile-up of GNDs. Then both CGs and FGs deform plastically in stage III, but CGs sustain higher strains again due to their higher dislocation accumulation capacity. Eventually, the difference in accommodating strains by CGs and FGs leads to strain partitioning.

The B-CNT/AA exhibits a further higher strength with superior YS and UTS of ~621 MPa and ~692 MPa, respectively, along with a ductility of ~2.6 at a strain rate of 1×10^{-4} s^{-1}. A high strengthening efficiency (η_s) of ~430% was achieved as calculated from,

$$\eta_s = \frac{\sigma_c - \sigma_m}{V_{CNT}\sigma_m}, \quad (2)$$

where σ_c and σ_m are the UTS of the composite and matrix, respectively. The formation of a proper amount of Al_4C_3 compound (Fig. 3) due to the reaction between Al matrix and CNTs would indicate robust interfacial bonding and load-transfer efficiency. Thus, the overall strength of B-CNT/AA increased. A close examination reveals that the tensile curves in Fig. 5(a) exhibit a unique phenomenon where an unusual elastic-plastic behavior appears in the upper elastic region as highlighted in dashed ellipses, along with the presence of plateau-like yield-point phenomenon which is usually referred to as Lüders deformation. The phenomenon is common in UFGed Al–Mg and Al–Cu–Mg alloys [23]. In the case of unimodal CNT-nanocomposite, this phenomenon is reported to be due to the non-linear behavior of CNTs, whereas in the present bimodal-grained Al alloys it has not yet been explored extensively but could be related to the coordination effect of CGs and UFGs.

Similar step-like phenomenon was observed in bimodal-grained materials in the plastic regime [19,32], but the physics behind this needs to be addressed. Such "two-step yielding" behavior was reported to be present in CNT-reinforced nanocomposites and not in their base alloys [33,34]. In contrast, both the materials in the present study (i.e., B-AA and B-CNT/AA) exhibited such phenomena (Fig. 5(a)), which is likely related to the distinct grain distribution (Fig. 4(a)). The peculiar behavior of two-step yielding in the present study could be attributed to: (i) distinct microstructure of CNT (fibrous) and matrix, (ii) bimodal grain distribution of the matrix, (iii) substantial difference in the strength of the reinforcement and heterogeneous/bimodal-grained matrix, and (iv) processing method. It is also possible that the annihilation of statistically stored dislocations could lead to such peculiar behavior [35].

A summary of tensile properties of commercial unimodal 2xxx Al alloys in heat-treated condition in comparison with the present B-AA is summarized in Fig. 6(a) [25,29,30,35–39]. It is seen that the present bimodal-grained structure possesses significantly higher strength with a fairly good ductility. The UTS vs. fracture strain of the present B-CNT/AA in comparison with those of CNT-reinforced Al–Cu nanocomposites made with different fabrication techniques along with their base alloys is summarized in Fig. 6(b) [11,25,29,30,33,35,38–41]. Such

Table 1
Tensile properties of bimodal-grained 2009Al and CNT/2009Al nanocomposite.

Specimen	Strain rate, s^{-1}	YS, MPa	UTS, MPa	Elongation, %	E, GPa
2009Al [29]	1×10^{-3}	299 ± 7.0	411 ± 10.0	12 ± 2.0	72.0
Bimodal-grained 2009Al	1×10^{-4}	553 ± 2.3	613 ± 6.4	10.8 ± 0.5	76.3 ± 2.7
	1×10^{-6}	543 ± 2.8	610 ± 3.0	11.1 ± 2.6	
Bimodal-grained CNT/2009Al	1×10^{-4}	621 ± 1.9	692 ± 25.7	2.6 ± 0.4	90.7 ± 3.5
	1×10^{-6}	585 ± 33.0	658 ± 16.1	2.9 ± 0.1	

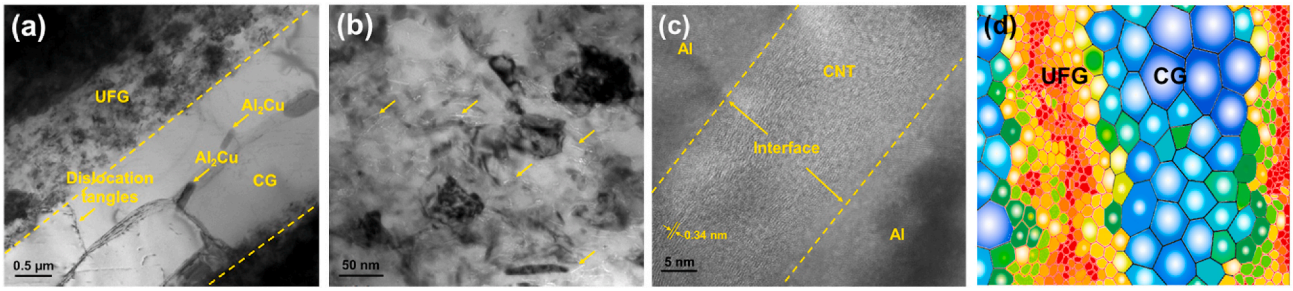

Fig. 4. TEM images showing **(a)** a bimodal grain distribution of UFG and CG bands and **(b)** singly dispersed CNTs in UFG zones, **(c)** HRTEM image showing the interface structure between Al matrix and CNTs, and **(d)** a schematic of bimodal-grained alloy consisting of layered UFG and CG.

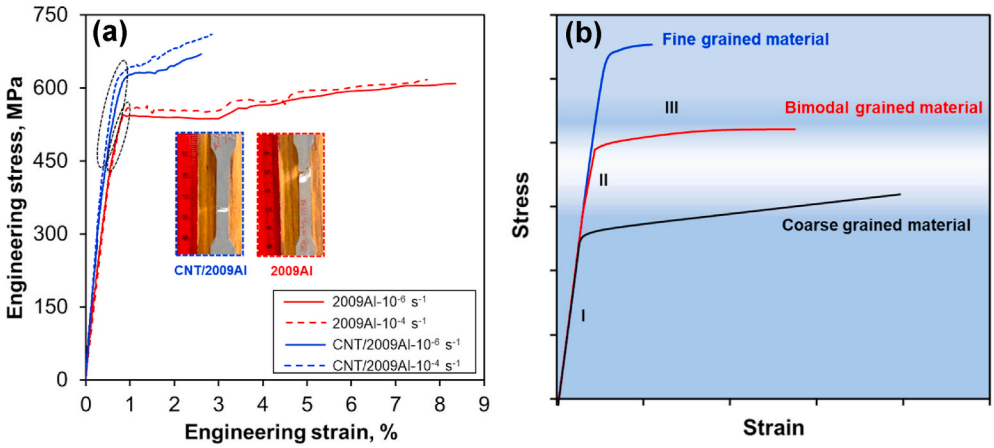

Fig. 5. **(a)** Typical tensile curves of bimodal-grained 2009Al and CNT/2009Al showing plateau-like regions in the curves at strain rates of 1×10^{-6} s^{-1} and 1×10^{-4} s^{-1}, and **(b)** a schematic representing the flow curve of bimodal-grained material.

superior strengths of the present B-AA and B-CNT/AA are extraordinary in the 2xxx Al composites. A similar analysis on the UTS vs. volume fraction of CNTs is presented in Fig. 6(c) [11,25,29,30,33,35,38–41]. Overall, the strength of the nanocomposites increases with increasing CNTs up to ~3 vol%, and then it starts to decrease. The reason behind the strength decrease with a higher amount of CNTs is mainly due to the agglomeration of CNTs [6,30]. It is evident that the UTS of the present B-AA and B-CNT/AA is positioned above that of the unimodal 2xxx Al alloys and their unimodal nanocomposites in Fig. 6(c).

The underlying strengthening mechanisms in CNT/Al nanocomposites were explored in Refs. [6,9,10,42,43]. The predominant strengthening mechanisms contributed by CNTs in the nanocomposites include load-transfer effect ($\Delta\sigma_{LT}$), Orowan strengthening ($\Delta\sigma_{OR}$), and dislocation strengthening ($\Delta\sigma_{DD}$) [8,44–48]. It is worth noting that if the grain structures in both base alloy and nanocomposite matrix are the same, the Hall-Petch equation concerning the grain boundary strengthening should not be considered. In the present study, the grain structures in both materials can be deemed to be similar due to the identical processing route and equivalent average grain sizes. Then the YS of the nanocomposite could be predicted as [44,45],

$$\sigma_{yc} = \sigma_{ym}\,(1+f_{LT})(1+f_{OR})(1+f_{DD}), \tag{3}$$

where σ_{ym} is the YS of matrix alloy, f_{LT}, f_{OR}, and f_{DD} are the improvement factors associated with load-transfer, Orowan, and thermal mismatch-induced dislocation strengthening, respectively, which are defined as the subsequent strength improvement (or increment) divided by σ_{ym} [44,45]. In other words, **Eq. (3)** can be re-written as,

$$\sigma_{yc} = \sigma_{ym}\left(1+\frac{\Delta\sigma_{LT}}{\sigma_{ym}}\right)\left(1+\frac{\Delta\sigma_{OR}}{\sigma_{ym}}\right)\left(1+\frac{\Delta\sigma_{DD}}{\sigma_{ym}}\right), \tag{4}$$

The load transfer would be a key strengthening mechanism in composites with aligned CNTs or fibers especially with high aspect ratios. But in the present nanocomposite, the actual length of the CNTs was observed to be in nano-meter range (Fig. 4(b)) and much smaller than the critical length (L_c = ~543–1628 nm) due to severe shearing effect during ball milling, as analyzed above. This would weaken the effect of load transfer although a sound bond was observed between Al matrix and CNTs (Fig. 4(c)). The improvement factor due to the load transfer is given in Ref. [8],

$$f_{LT} = \frac{V_p}{2}, \tag{5}$$

where V_p is the volume fraction of reinforcement particles (i.e., the volume fraction of CNTs in this study). The dislocation movement can be impeded by hard impenetrable CNTs by forming dislocation loops due to the strong C–C bonds and high strength of CNTs. A schematic diagram in Fig. 7(a) illustrates the formation of Orowan loops which lead to an increase in the strength of nanocomposites. As the dislocations in the Al matrix glide over the slip plane, they leave Orowan loops in their wake after interacting with and bypassing the CNTs. A higher stress is needed to drive more dislocations to bypass CNTs with more Orowan loops left around CNTs, thus leading to an increase in the strength of the material. Xu et al. [46] detected similar dislocation loops around the CNTs in an aluminum matrix via TEM, showing the characteristics of Orowan strengthening. In particular, the Orowan looping was directly spotted via *in-situ* TEM observations along with molecular dynamics (MD) simulations, where the dislocations were pinned by CNTs [47]. Chen et al. [48] also observed via TEM some dislocation loops containing two face-to-face dislocations locating along the same lattice plane in a pure copper matrix composites reinforced with CNT-graphene hybrids. An atomic-level analysis of strengthening mechanisms in aluminum matrix

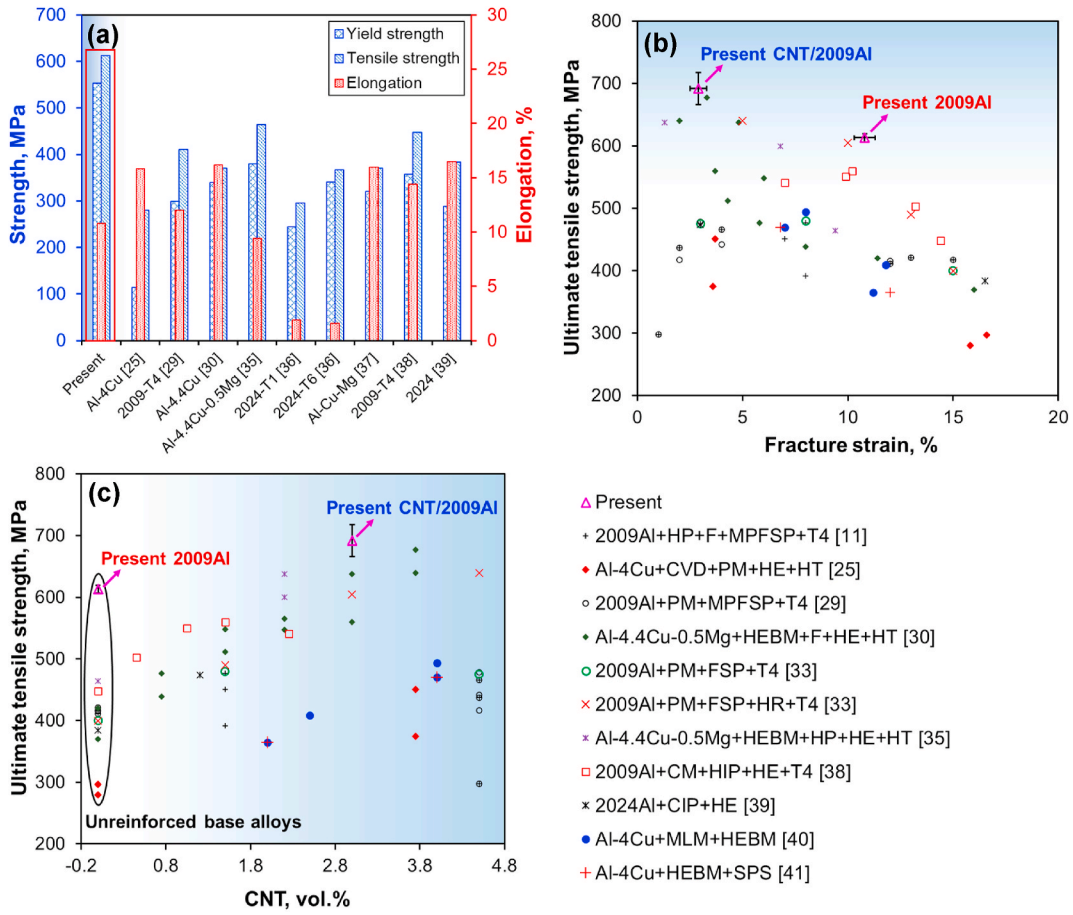

Fig. 6. **(a)** Tensile properties of the present bimodal-grained 2009Al alloy in T4 condition in comparison with other commercial 2xxx Al alloys, **(b)** ultimate tensile strength vs. fracture strain of the present material in comparison with various CNT-reinforced 2xxx Al composites, and **(c)** ultimate tensile strength of CNT-reinforced 2xxx Al nanocomposites with varying CNT contents along with the present 3 vol%CNT/2009Al nanocomposite.

composites reinforced by aligned CNTs via MD simulations also uncovered the presence of Orowan looping even for long CNTs due to dislocations bowing around CNTs [49]. Furthermore, even though the MMNCs are reinforced by graphene (being a single layer of carbon atoms arranged in a two-dimensional honeycomb lattice), it has also been concluded that the most effective strengthening mechanisms are the mismatch of thermal expansion between the matrix and graphene and the Orowan looping mechanism [50]. The improvement factor due to Orowan looping strengthening is given by Orowan-Ashby equation [51],

$$f_{OR} = \frac{0.84 M G_m b}{\sigma_{ym} \pi d_{eq} \sqrt{(1-\nu)} \left(\sqrt{\frac{3\pi}{2V_p}} - \frac{\pi}{4} \right)} \ln\left(\frac{\pi d_{eq}}{8b}\right), \tag{6}$$

where M is the Taylor factor (3.06 for FCC [12]), G_m is the shear modulus of matrix calculated as $G_m = E_m/[2 \times (1+\nu)]$, ν is the Poisson's ratio of aluminum matrix alloy (0.33 [52]), d_{eq} is the equivalent size of CNTs obtained using a spherical model [6]. All the values used in the calculations are listed in Table 2, where the equivalent diameter of CNTs could be obtained from the following equation,

$$d_{eq} = \sqrt[3]{\frac{3}{2} L_{CNT} d_{CNT}^2}, \tag{7}$$

where L_{CNT} and d_{CNT} are the average length and diameter of CNTs (~15 nm is used in calculations). Then $\Delta\sigma_{OR}$ is obtained to be ~69 MPa, suggesting that it is an important strengthening mechanism. Orowan strengthening and thermal mismatch were also reported by Yoo et al. [13] as the main mechanisms for strengthening their CNT/Al nanocomposites. They also reported shortening of CNTs by ball milling and suggested that the shorter fragments helped achieve the critical inter-particle distance for effective Orowan strengthening. CNTs in the nanocomposite cause prismatic punching of dislocations at the interface and increase the work hardening of the material. Thus, the third strengthening improvement factor from the increased dislocation density can be expressed as,

$$f_{DD} = \frac{k G_m b \sqrt{\Delta\rho}}{\sigma_{ym}}, \tag{8}$$

where k is a constant (~1.25 [44]) and $\Delta\rho$ is the increased dislocation density, stemming from the particle/matrix thermal mismatch-induced additional dislocations in the composite relative to base alloy. The dislocation density increment of the present nanocomposite with respect to its base alloy has been obtained via XRD analysis to be 8.4×10^{12} m^{-2}. The $\Delta\sigma_{DD}$ is then estimated to be 29.7 MPa. Such a significant increment is related to the smaller diameter and aspect ratio of CNTs [42]. To further examine the effect of volume fraction of CNTs on the dislocation strengthening, the enhanced dislocation density in composite relative to base alloy can be calculated as [44],

$$\Delta\rho = \frac{12 \Delta\alpha \Delta T V_p}{b d_{eq} (1 - V_p)}, \tag{9}$$

$$\Delta\alpha = \alpha_m - \alpha_p;\ \Delta T = T_{process} - T_{test}, \tag{9a}$$

where α_m and α_p are the coefficients of thermal expansion of the matrix (~2.3×10^{-5} K^{-1} [10]) and reinforcement particles (~2.1×10^{-5} K^{-1}

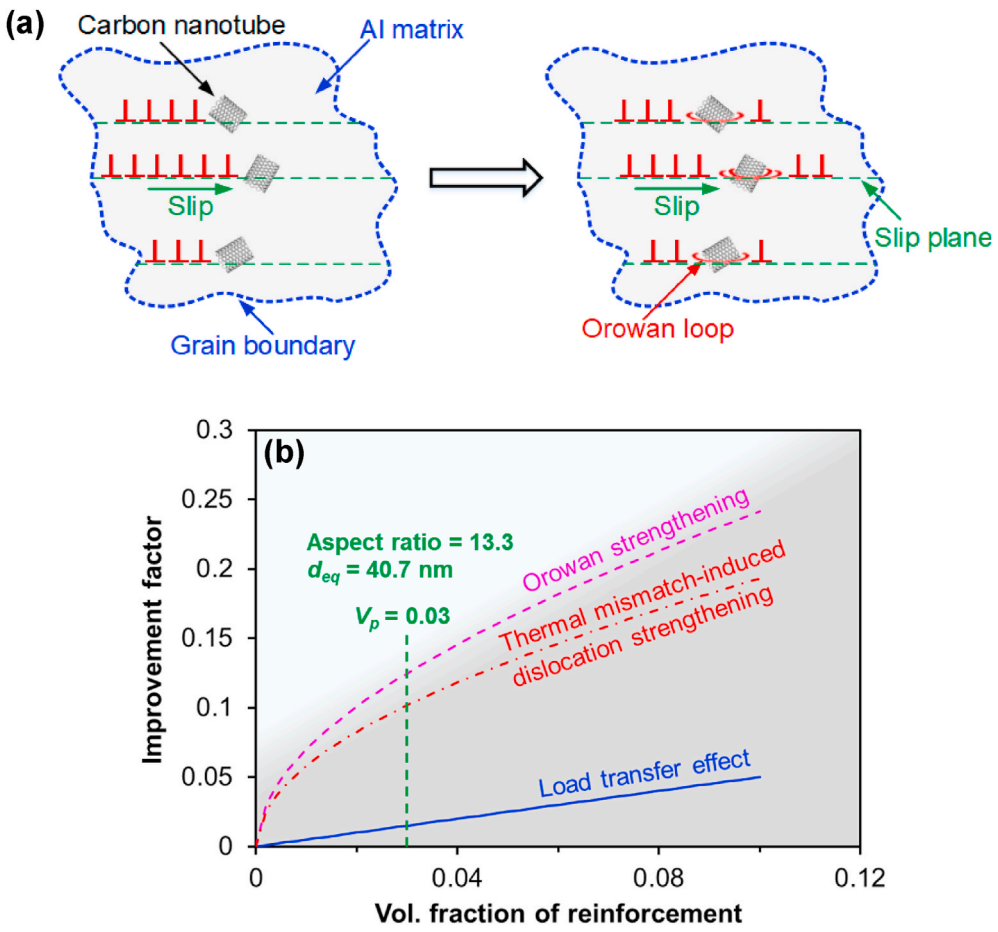

Fig. 7. (a) A schematic showing the Orowan looping mechanism after dislocations gliding and bypassing the CNTs, and **(b)** the individual contribution of strengthening mechanisms in the nanocomposite as a function of volume fraction.

Table 2
Parameters used in the calculation of strengthening mechanisms.

Parameter	Value	Units	Ref.
M	3.06	–	[12]
b	0.286	nm	–
k	1.25	–	[44]
d_{CNT} (or d_p)	15	nm	[23]
d_{eq}	40.7	nm	Exp.
E_m	76.3	GPa	Exp.
G_m	28.7	GPa	Exp.
L_{CNT}	200	nm	[23]
V_{CNT} (or V_p)	0.03	–	Exp.
ν	0.33	–	[52]
α_m	2.3×10^{-5}	K^{-1}	[10]
α_p	2.1×10^{-5}	K^{-1}	[10]
σ_{CNT}	30	GPa	[31]
σ_{ym}	553	MPa	Exp.

[10]), respectively, and $T_{process}$ and T_{test} are the processing and test temperatures, respectively. In the present multi-step processing route, $T_{process}$ is taken as the last step processing high temperature (i.e., the solution temperature of 500 °C) at which the reinforcement particles and matrix are considered to be in an equilibrium condition without any push to each other. Then, Eq. (8) can then be re-written as,

$$f_{DD} = \frac{4.33G_m}{\sigma_{ym}}\sqrt{\frac{b\Delta\alpha\Delta T V_p}{d_{eq}(1-V_p)}}. \quad (10)$$

It should be noted that the increased dislocations, reflected by the presence of residual stresses in composites, are in essence attributed to the difference in the coefficients of thermal expansion between the matrix and reinforcement. With the combination of aforementioned strengthening effects, the predicted YS of the nanocomposite using Eq. (3) is evaluated to be 665 MPa, which is in close agreement with the experimental YS of ~621 MPa with a deviation of ~7.1%. The reason for the lower value of experimental YS could be due to the presence of potential porosity and the absence of CNTs in CGs, which are not considered in the strengthening calculations. The individual contribution of these strengthening mechanisms with respect to the volume fraction of CNTs is presented in Fig. 7(b). All the contribution factors calculated using Eqs (5), (6) and (10) increase with increasing volume fraction. The strengthening contribution is relatively low from the load transfer, and is pretty high from the Orowan strengthening, while the contribution of thermal mismatch-inducing dislocation strengthening lies in the middle. It should be pointed out that the relatively low load transfer contribution is related to the equivalent spherical particle consideration. Further modeling by integrating the aspect ratio of CNTs (or other reinforcement particles) into the strengthening factors needs to be developed. Finally, the overall high strength of the present nanocomposite is a result of the coupled effects of these nanocomposite-specific strengthening mechanisms along with the bimodal grain distribution generated via the multi-step processing route consisting of HEBM, vacuum hot pressing, extrusion, and T4 heat treatment. Thus, CNT-reinforced bimodal-grained nanocomposites are promising candidates for achieving superior mechanical performance with balanced high strength and ductility.

5. Conclusions

In this study, a CNT-reinforced bimodal-grained 2009Al nanocomposite along with its base alloy was fabricated by two-step high energy ball milling, hot pressing, extrusion followed by T4 heat treatment. A relationship between the bimodal-grained microstructure and mechanical properties in the base alloy was first established and its strengthening effect was analyzed. The simultaneous presence of UFGs and CGs with a high dislocation density led to an excellent strength-ductility harmony in the bimodal-grained alloy. Singly-dispersed CNTs were present in the UFG regime of the nanocomposite, whereas the CG region aligned along the ED was basically free from CNTs. The bimodal grain distribution and size were observed to be equivalent with a similar strong fiber texture along <111>//ED in the nanocomposite matrix and base alloy. An addition of 3 vol% CNTs led to a high UTS of ~692 MPa, compared with that of ~613 MPa in the bimodal-grained base alloy. An unusual elastic-plastic behavior appeared in the elastic region along with the presence of plateau-like yield-point phenomenon in both base alloy and nanocomposite. Predominant Orowan strengthening mechanism was identified along with load-transfer and thermal mismatch-induced dislocation strengthening mechanisms in the CNT/Al nanocomposite. The predicted yield strength of the nanocomposite was in close agreement with the experimental value.

CRediT authorship contribution statement

S.M.A.K. Mohammed: Data curation, Formal analysis, Investigation, Methodology, Validation, Writing – original draft. **D.L. Chen:** Conceptualization, Funding acquisition, Methodology, Resources, Supervision, Writing – review & editing. **Z.Y. Liu:** Methodology, Validation, Writing – review & editing. **D.R. Ni:** Methodology, Writing – review & editing. **Q.Z. Wang:** Methodology, Writing – review & editing. **B.L. Xiao:** Methodology, Resources, Writing – review & editing. **Z.Y. Ma:** Funding acquisition, Methodology, Resources, Writing – review & editing.

Declaration of competing interest

The authors declare that they have no known competing financial interests or personal relationships that could have appeared to influence the work reported in this paper.

Acknowledgements

The authors would like to thank the Natural Sciences and Engineering Research Council of Canada (NSERC) and the National Natural Science Foundation of China (Nos. 51931009, 51871214, 51871215) in the form of international research collaboration. Z.Y. Liu, D.R. Ni, Q.Z. Wang, B.L. Xiao, Z.Y. Ma further thank Key Research Program of Frontier Sciences, CAS (No. QYZDJ-SSW-JSC015) and National Key R&D Program of China (No. 2017YFB0703104). The authors would also like to thank Messrs. Q. Li, A. Machin, J. Amankrah and R. Churaman for their assistance.

Appendix A. Supplementary data

Supplementary data to this article can be found online at https://doi.org/10.1016/j.msea.2021.141370.

Data availability

The raw/processed data required to reproduce these findings cannot be shared at this time as the data also forms part of an ongoing study.

References

[1] X. Zhou, Z. Feng, L. Zhu, J. Xu, L. Miyagi, H. Dong, H. Sheng, Y. Wang, Q. Li, Y. Ma, H. Zhang, J. Yan, N. Tamura, M. Kunz, K. Lutker, T. Huang, D.A. Hughes, X. Huang, B. Chen, High-pressure strengthening in ultrafine-grained metals, Nature 579 (2020) 67–72, https://doi.org/10.1038/s41586-020-2036-z.
[2] T.-C. Lin, C. Cao, M. Sokoluk, L. Jiang, X. Wang, J.M. Schoenung, E.J. Lavernia, X. Li, Aluminum with dispersed nanoparticles by laser additive manufacturing, Nat. Commun. 10 (2019) 4124, https://doi.org/10.1038/s41467-019-12047-2.
[3] X. Fu, Z. Yu, Z. Tan, G. Fan, P. Li, M. Wang, D.-B. Xiong, Z. Li, Enhanced strain hardening by bimodal grain structure in carbon nanotube reinforced Al–Mg composites, Mater. Sci. Eng. 803 (2021) 140726, https://doi.org/10.1016/j.msea.2020.140726.
[4] Y. Bai, R. Zhang, X. Ye, Z. Zhu, H. Xie, B. Shen, D. Cai, B. Liu, C. Zhang, Z. Jia, S. Zhang, X. Li, F. Wei, Carbon nanotube bundles with tensile strength over 80 GPa, Nat. Nanotechnol. 13 (2018) 589–595, https://doi.org/10.1038/s41565-018-0141-z.
[5] K. Ma, Z.Y. Liu, B.S. Liu, B.L. Xiao, Z.Y. Ma, Improving ductility of bimodal carbon nanotube/2009Al composites by optimizing coarse grain microstructure via hot extrusion, Compos. Part A Appl. Sci. Manuf. 140 (2021) 106198, https://doi.org/10.1016/j.compositesa.2020.106198.
[6] S.M.A.K. Mohammed, D.L. Chen, Carbon nanotube-reinforced aluminum matrix composites, Adv. Eng. Mater. 22 (2020) 1901176, https://doi.org/10.1002/adem.201901176.
[7] M. Wang, Y. Li, B. Chen, D. Shi, J. Umeda, K. Kondoh, J. Shen, The rate-dependent mechanical behavior of CNT-reinforced aluminum matrix composites under tensile loading, Mater. Sci. Eng. 808 (2021) 140893, https://doi.org/10.1016/j.msea.2021.140893.
[8] R. George, K.T.T. Kashyap, R. Rahul, S. Yamdagni, Strengthening in carbon nanotube/aluminium (CNT/Al) composites, Scripta Mater. 53 (2005) 1159–1163, https://doi.org/10.1016/j.scriptamat.2005.07.022.
[9] F. Mokdad, D.L. Chen, Z.Y. Liu, B.L. Xiao, D.R. Ni, Z.Y. Ma, Deformation and strengthening mechanisms of a carbon nanotube reinforced aluminum composite, Carbon 104 (2016) 64–77, https://doi.org/10.1016/j.carbon.2016.03.038.
[10] J.G. Park, D.H. Keum, Y.H. Lee, Strengthening mechanisms in carbon nanotube-reinforced aluminum composites, Carbon 95 (2015) 690–698, https://doi.org/10.1016/j.carbon.2015.08.112.
[11] Z.Y. Liu, B.L. Xiao, W.G. Wang, Z.Y. Ma, Singly dispersed carbon nanotube/aluminum composites fabricated by powder metallurgy combined with friction stir processing, Carbon 50 (2012) 1843–1852, https://doi.org/10.1016/j.carbon.2011.12.034.
[12] B. Chen, J. Shen, X. Ye, L. Jia, S. Li, J. Umeda, M. Takahashi, K. Kondoh, Length effect of carbon nanotubes on the strengthening mechanisms in metal matrix composites, Acta Mater. 140 (2017) 317–325, https://doi.org/10.1016/j.actamat.2017.08.048.
[13] S.J. Yoo, S.H. Han, W.J. Kim, Strength and strain hardening of aluminum matrix composites with randomly dispersed nanometer-length fragmented carbon nanotubes, Scripta Mater. 68 (2013) 711–714, https://doi.org/10.1016/j.scriptamat.2013.01.013.
[14] P. Kumar, M. Kawasaki, T.G. Langdon, Review: overcoming the paradox of strength and ductility in ultrafine-grained materials at low temperatures, J. Mater. Sci. 51 (2016) 7–18, https://doi.org/10.1007/s10853-015-9143-5.
[15] Y. Zhu, K. Ameyama, P.M. Anderson, I.J. Beyerlein, H. Gao, H.S. Kim, E. Lavernia, S. Mathaudhu, H. Mughrabi, R.O. Ritchie, N. Tsuji, X. Zhang, X. Wu, Heterostructured materials: superior properties from hetero-zone interaction, Mater. Res. Lett. 9 (2021) 1–31, https://doi.org/10.1080/21663831.2020.1796836.
[16] X.H. Du, W.P. Li, H.T. Chang, T. Yang, G.S. Duan, B.L. Wu, J.C. Huang, F.R. Chen, C.T. Liu, W.S. Chuang, Y. Lu, M.L. Sui, E.W. Huang, Dual heterogeneous structures lead to ultrahigh strength and uniform ductility in a Co-Cr-Ni medium-entropy alloy, Nat. Commun. 11 (2020) 2390, https://doi.org/10.1038/s41467-020-16085-z.
[17] X. Wu, Y. Zhu, Heterogeneous materials: a new class of materials with unprecedented mechanical properties, Mater. Res. Lett. 5 (2017) 527–532, https://doi.org/10.1080/21663831.2017.1343208.
[18] K. Lu, Making strong nanomaterials ductile with gradients, Science 345 (2014) 1455–1456, https://doi.org/10.1126/science.1255940.
[19] B.B. He, B. Hu, H.W. Yen, G.J. Cheng, Z.K. Wang, H.W. Luo, M.X. Huang, High dislocation density–induced large ductility in deformed and partitioned steels, Science 357 (2017) 1029–1032, https://doi.org/10.1126/science.aan0177.
[20] R. Valiev, Nanostructuring of metals by severe plastic deformation for advanced properties, Nat. Mater. 3 (2004) 511–516, https://doi.org/10.1038/nmat1180.
[21] D. Witkin, Z. Lee, R. Rodriguez, S. Nutt, E. Lavernia, Al–Mg alloy engineered with bimodal grain size for high strength and increased ductility, Scripta Mater. 49 (2003) 297–302, https://doi.org/10.1016/S1359-6462(03)00283-5.
[22] X. Wu, M. Yang, F. Yuan, G. Wu, Y. Wei, X. Huang, Y. Zhu, Heterogeneous lamella structure unites ultrafine-grain strength with coarse-grain ductility, Proc. Natl. Acad. Sci. Unit. States Am. 112 (2015) 14501–14505, https://doi.org/10.1073/pnas.1517193112.
[23] Z.Y. Liu, K. Ma, G.H. Fan, K. Zhao, J.F. Zhang, B.L. Xiao, Z.Y. Ma, Enhancement of the strength-ductility relationship for carbon nanotube/Al–Cu–Mg nanocomposites by material parameter optimisation, Carbon N. Y. 157 (2020) 602–613, https://doi.org/10.1016/j.carbon.2019.10.080.
[24] X. Chen, G. Zhao, G. Liu, L. Sun, L. Chen, C. Zhang, Microstructure evolution and mechanical properties of 2196 Al-Li alloy in hot extrusion process, J. Mater.

Process. Technol. 275 (2020) 116348, https://doi.org/10.1016/j.jmatprotec.2019.116348.
[25] X. Meng, T. Liu, C. Shi, E. Liu, C. He, N. Zhao, Synergistic effect of CNTs reinforcement and precipitation hardening in in-situ CNTs/Al–Cu composites, Mater. Sci. Eng. 633 (2015) 103–111, https://doi.org/10.1016/j.msea.2015.03.007.
[26] R. Chierchia, T. Böttcher, H. Heinke, S. Einfeldt, S. Figge, D. Hommel, Microstructure of heteroepitaxial GaN revealed by x-ray diffraction, J. Appl. Phys. 93 (2003) 8918–8925, https://doi.org/10.1063/1.1571217.
[27] R. Xu, Z. Tan, D. Xiong, G. Fan, Q. Guo, J. Zhang, Y. Su, Z. Li, D. Zhang, Balanced strength and ductility in CNT/Al composites achieved by flake powder metallurgy via shift-speed ball milling, Compos. Part A Appl. Sci. Manuf. 96 (2017) 57–66, https://doi.org/10.1016/j.compositesa.2017.02.017.
[28] C. Suryanarayana, N. Al-Aqeeli, Mechanically alloyed nanocomposites, Prog. Mater. Sci. 58 (2013) 383–502, https://doi.org/10.1016/j.pmatsci.2012.10.001.
[29] Z.Y. Liu, B.L. Xiao, W.G. Wang, Z.Y. Ma, Analysis of carbon nanotube shortening and composite strengthening in carbon nanotube/aluminum composites fabricated by multi-pass friction stir processing, Carbon N. Y. 69 (2014) 264–274, https://doi.org/10.1016/j.carbon.2013.12.025.
[30] N.S. Anas, R.K. Dash, T.N. Rao, R. Vijay, Effect of carbon nanotubes as reinforcement on the mechanical properties of aluminum-copper-magnesium alloy, J. Mater. Eng. Perform. 26 (2017) 3376–3386, https://doi.org/10.1007/s11665-017-2730-7.
[31] H. Choi, J. Shin, B. Min, J. Park, D. Bae, Reinforcing effects of carbon nanotubes in structural aluminum matrix nanocomposites, J. Mater. Res. 24 (2009) 2610–2616, https://doi.org/10.1557/jmr.2009.0318.
[32] R. Ma, C. Peng, Z. Cai, R. Wang, Z. Zhou, X. Li, X. Cao, Effect of bimodal microstructure on the tensile properties of selective laser melt Al-Mg-Sc-Zr alloy, J. Alloys Compd. 815 (2020) 152422, https://doi.org/10.1016/j.jallcom.2019.152422.
[33] Z.Y. Liu, B.L. Xiao, W.G. Wang, Z.Y. Ma, Developing high-performance aluminum matrix composites with directionally aligned carbon nanotubes by combining friction stir processing and subsequent rolling, Carbon 62 (2013) 35–42, https://doi.org/10.1016/j.carbon.2013.05.049.
[34] K.T. Kim, S. Il Cha, S.H. Hong, S.H. Hong, Microstructures and tensile behavior of carbon nanotube reinforced Cu matrix nanocomposites, Mater. Sci. Eng. 430 (2006) 27–33, https://doi.org/10.1016/j.msea.2006.04.085.
[35] N.S. Anas, M. Ramakrishna, R. Vijay, Microstructural characteristics and mechanical properties of CNT/Ni coated CNT–dispersed Al alloys produced by high energy ball milling and hot extrusion, Met. Mater. Int. 26 (2020) 272–283, https://doi.org/10.1007/s12540-019-00327-x.
[36] D.P. Bishop, W.F. Caley, G.J. Kipouros, R.L. Hexemer, I.W. Donaldson, Powder metallurgy processing of 2xxx and 7xxx series aluminium alloys, Can. Metall. Q. 50 (2011) 246–252, https://doi.org/10.1179/1879139511Y.0000000003.
[37] E. Khafizova, R. Islamgaliev, V. Sitdikov, Strength and fatigue of an ultrafine-grained Al-Cu-Mg alloy, MATEC Web Conf 129 (2017), https://doi.org/10.1051/matecconf/201712902039, 02039.
[38] T. He, X. He, P. Tang, D. Chu, X. Wang, P. Li, The use of cryogenic milling to prepare high performance Al2009 matrix composites with dispersive carbon nanotubes, Mater. Des. 114 (2017) 373–382, https://doi.org/10.1016/j.matdes.2016.11.008.
[39] C. Deng, X. Zhang, D. Wang, Q. Lin, A. Li, Preparation and characterization of carbon nanotubes/aluminum matrix composites, Mater. Lett. 61 (2007) 1725–1728, https://doi.org/10.1016/j.matlet.2006.07.119.
[40] D.H. Nam, S.I. Cha, B.K. Lim, H.M. Park, D.S. Han, S.H. Hong, Synergistic strengthening by load transfer mechanism and grain refinement of CNT/Al–Cu composites, Carbon 50 (2012) 2417–2423, https://doi.org/10.1016/j.carbon.2012.01.058.
[41] D.H. Nam, Y.K. Kim, S.I. Cha, S.H. Hong, Effect of CNTs on precipitation hardening behavior of CNT/Al–Cu composites, Carbon 50 (2012) 4809–4814, https://doi.org/10.1016/j.carbon.2012.06.005.
[42] S. Dong, J. Zhou, D. Hui, A quantitative understanding on the mechanical behaviors of carbon nanotube reinforced nano/ultrafine-grained composites, Int. J. Mech. Sci. 101– 102 (2015) 29–37, https://doi.org/10.1016/j.ijmecsci.2015.07.019.
[43] K. Xie, G. Zhang, H. Huang, J. Zhang, Z. Liu, B. Cai, Investigation of the main strengthening mechanism of carbon nanotube reinforced aluminum composites, Mater. Sci. Eng. 804 (2021) 140780, https://doi.org/10.1016/j.msea.2021.140780.
[44] Z. Zhang, D.L. Chen, Consideration of Orowan strengthening effect in particulate-reinforced metal matrix nanocomposites: a model for predicting their yield strength, Scripta Mater. 54 (2006) 1321–1326, https://doi.org/10.1016/j.scriptamat.2005.12.017.
[45] Z. Zhang, D.L. Chen, Contribution of Orowan strengthening effect in particulate-reinforced metal matrix nanocomposites, Mater. Sci. Eng. (2008) 483–484, https://doi.org/10.1016/j.msea.2006.10.184, 148–152.
[46] Z.Y. Xu, C.J. Li, K.R. Li, J.H. Yi, J.J. Tang, Q.X. Zhang, X.Q. Liu, R. Bao, X. Li, Carbon nanotube-reinforced aluminum matrix composites enhanced by grain refinement and in situ precipitation, J. Mater. Sci. 54 (2019) 8655–8664, https://doi.org/10.1007/s10853-019-03411-0.
[47] K.P. So, X. Liu, H. Mori, A. Kushima, J.G. Park, H.S. Kim, S. Ogata, Y.H. Lee, J. Li, Ton-scale metal–carbon nanotube composite: the mechanism of strengthening while retaining tensile ductility, Extrem. Mech. Lett. 8 (2016) 245–250, https://doi.org/10.1016/j.eml.2016.04.002.
[48] X. Chen, J. Tao, Y. Liu, R. Bao, F. Li, C. Li, J. Yi, Interface interaction and synergistic strengthening behavior in pure copper matrix composites reinforced with functionalized carbon nanotube-graphene hybrids, Carbon N. Y. 146 (2019) 736–755, https://doi.org/10.1016/j.carbon.2019.02.048.
[49] J. Xiang, L. Xie, S.A. Meguid, S. Pang, J. Yi, Y. Zhang, R. Liang, An atomic-level understanding of the strengthening mechanism of aluminum matrix composites reinforced by aligned carbon nanotubes, Comput. Mater. Sci. 128 (2017) 359–372, https://doi.org/10.1016/j.commatsci.2016.11.032.
[50] M. Dadkhah, A. Saboori, P. Fino, An overview of the recent developments in metal matrix nanocomposites reinforced by graphene, Materials 12 (2019) 2823, https://doi.org/10.3390/ma12172823.
[51] T. Lu, C. Chen, P. Li, C. Zhang, W. Han, Y. Zhou, C. Suryanarayana, Z. Guo, Enhanced mechanical and electrical properties of in situ synthesized nano-tungsten dispersion-strengthened copper alloy, Mater. Sci. Eng. 799 (2021) 140161, https://doi.org/10.1016/j.msea.2020.140161.
[52] R. Xu, Z. Tan, G. Fan, G. Ji, Z. Li, Q. Guo, Z. Li, D. Zhang, Microstructure-based modeling on structure-mechanical property relationships in carbon nanotube/aluminum composites, Int. J. Plast. 120 (2019) 278–295, https://doi.org/10.1016/j.ijplas.2019.05.006.